CrossMark

Investigations on electrical and energy storage behaviour of PZN-PT, PMN-PT, PZN–PMN-PT piezoelectric solid solutions

Rajesh Narayana Perumal[1,2] · Venkatraj Athikesavan[1,2]

Abstract

Electrical response and energy storage behaviour of PZN-PT, PMN-PT, PZN–PMN-PT (PZN-$PbZn_{1/3}Nb_{2/3}O_3$, PMN-$PbMg_{1/3}Nb_{2/3}O_3$ and PT-$PbTiO_3$) solid solutions were investigated. SEM micrographs of the sample showed grains of unequal sizes distributed throughout the sample. The average grain size observed was about 0.77 µm for PZN-PT, 0.93 for PMN-PT and 1.82 for PZN–PMN-PT solid solutions. All the solid solutions exhibited good dielectric relaxation behaviour up to 500 °C in the frequency range of 1–2 MHz. The solid solutions showed improved ferroelectric properties (P_r ~ 17.4 µC cm^{-2}, E_c ~ 3.65 kV cm^{-1}, P_m ~ 20.1 µC cm^{-2} for PZN-PT) and crossover from nonergodic to ergodic relaxor phase with respect to temperature. The optimum piezoelectric coefficients, the piezoelectric voltage coefficients of the solid solutions were also studied. P–E loop analysis confirmed high energy storage density (W) of 0.25 J cm^{-3} at 50 kV cm^{-1} for PZN–PMN-PT which substantiates its wide use in capacitor applications.

1 Introduction

In recent years, lead-containing complex perovskite solid solutions have been explored and utilized widely owing to exceptional characteristics that meet the demands for innovations in a multitude of industrial applications [1, 2]. Lead-based ferroelectric solid solutions have been intensively studied over the past decades owing to their advanced applications in sensors, large strain actuators, microelectronics, capacitors, ultrasonic motors, non-volatile memories, high-frequency transducers and energy harvesters [3–5]. The lead-based piezoelectric solid solutions exhibit excellent ferroelectric and piezoelectric properties and have been potentially used in applications such as perovskite relaxor and electronic device market worldwide [6–9]. However, the energy storage density of these solid solutions materials is much lower than that of polymers due to their low dielectric breakdown strengths, which in turn limits their applications for energy storage applications [10–12]. Among the family of lead-based relaxor ferroelectric solid solution,

PZN-PT, PMN-PT, PZN–PMN-PT are the most important representatives of relaxor-based perovskite frameworks, which are exhibiting excellent piezoelectric performance close to the morphotropic phase boundary (MPB) [13–15]. Large piezoelectric coefficients are achieved by incorporation of substituent or additives in compositions near the morphotropic phase boundaries. Lead-based relaxor ferroelectric solid solutions have perovskite structure (ABO_3) and form a solid solution with other alkaline or alkaline-earth cations, with altered properties suitable for various applications [16]. The physical properties of the lead-based solid solutions are achieved by suppressing or promoting oxygen or cation vacancies, as presence of these vacancies in perovskite structure is a very important parameter to control its physical properties. Often the inclusion of acceptor or donor dopants is used to change the physical properties of lead-based solid solutions [17]. In general, chemical formulas are written as, B $(Y_1Y_2)O_3$ and B $(Y_1Y_2)O_3$-$PbTiO_3$ (where B site is usually occupied by lead, Y_1 site is occupied by Mg^{2+}, Fe^{3+}, Sc^{3+}, Yb^{3+}, Zn^{2+}, Ni^{2+}, In^{3+}, etc., and the Y_2 site is occupied by Ta^{5+}, Nb^{5+}, W^{6+}, etc., [18, 19]). These can form multiple ferroelectric solid solutions due to the variation of Y site element; however, most of these solid solutions are unable to be meet the requirements at present, therefore, only a few solid solutions are available in practice [20]. It is hard to exclude the influence of defects in the electrical properties caused by acceptor or donor doping of the material. Relaxor ferroelectric

✉ Rajesh Narayana Perumal
   rajeshnp@ssn.edu.in

1 Department of Physics, SSN College of Engineering, Kalavakkam 603 110, India

2 Center for Radiation, Environmental Science and Technology, SSN College of Engineering, Kalavakkam 603110, India

behaviour has been reported in a variety of perovskite systems such as $Pb(In_{1/2}Nb_{1/2})O_3$–$Pb(Zn_{1/3}Nb_{2/3})O_3$–$PbTiO_3$ [21], $Pb(Mg_{1/3}Nb_{2/3})O_3$–$Pb(Yb_{1/2}Nb_{1/2})O_3$–$PbTiO_3$ [22], $Pb(Co_{1/2}W_{1/2})O_3$–$Pb(Mn_{1/2}Nb_{2/3})O_3$–$Pb(Zr, Ti)O_3$ [23], $Pb_{0.95}Pr_{0.05}Zr_{0.52}Ti_{0.48}O_3$-$CoPr_{0.1}Fe_{1.9}O_4$ [24], $Pb(Lu_{1/2}Nb_{1/2})O_3$–$PbTiO_3$ [25], $PbTiO_3$–$PbZrO_3$–$PbNb_{2/3}Mg_{1/3}O_3$–$PbGeO_3$ [26], $(Pb_{0.97}La_{0.02})(Zr_{0.95}Ti_{0.05})O_3$ [27], $Pb(Mg_{1/3}Nb_{2/3})O_3$–$Pb(Sn_{0.46}Ti_{0.54})O_3$ [28], $PbHfO_3$–$PbTiO_3$–$Pb(Mg_{1/3}Nb_{2/3})O_3$ [29], $PbSnO_3$–$PbTiO_3$–$Pb(Mg_{1/3}Nb_{2/3})O_3$ [30] and $Pb(In_{1/2}Nb_{1/2})O_3$–$Pb(Mg_{1/3}Nb_{2/3})O_3$–$PbTiO_3$ [31] which are different from normal ferroelectric behaviors due to the composition variations of the perovskite structure. These lead-based solid solutions have interesting physical properties which are potential for electronic device applications [32]. PZT ($PbZr_{1-x}Ti_xO_3$) based solid solutions have been given much attention due to their excellent piezoelectric coefficient at the range of (d_{33} ~ 200–750 pC N^{-1}) and high Curie temperature (T_C ~ 180–320 °C) and are currently used in many electronic devices. In this work, investigation of inorganic lead-based perovskite relaxor ferroelectric solid solutions such as lead zinc niobate-lead titanate, $Pb(Zn_{1/3}Nb_{2/3})O_3$–$PbTiO_3$ (PZN-PT), lead magnesium niobate-lead titanate $Pb(Mg_{1/3}Nb_{2/3})O_3$–$PbTiO_3$ (PMN-PT), and lead magnesium niobate-lead zinc niobate-lead titanate, $Pb(Zn_{1/3}Nb_{2/3})O_3$–$Pb(Mg_{1/3}Nb_{2/3})O_3$–$PbTiO_3$ (PZN–PMN-PT) solid solutions are reported and investigated at near morphotropic phase boundary. Their ternary compound has secured a maximum place in the field of materials science and engineering due to excellent energy storage properties for capacitor applications. The ferroelectric properties are observed when lead-based solid solutions are combined with lead titanate, leading to an increase in the Curie temperature and a subsequent increase in the spontaneous polarization of the material [33]. Large piezoelectric coefficients, which could be improved by incorporation of substituent or additives, were obtained for compositions near the morphotropic phase boundaries. At times, lower symmetric ferroelectric phases can be responsible for large piezoelectric activity exhibited by this solid solution. In this regard, several interesting approaches involving physical, chemical and microstructure modifications of the dielectric lead-based solid solutions are adopted.

This paper depicts dielectric, piezoelectric, ferroelectric and energy storage properties of PZN-PT, PMN-PT, PZN–PMN-PT solid solutions, which are potential candidates for capacitor applications.

2 Experimental procedure

2.1 Synthesis of the solid solutions obtained by solid-state reaction

Three types of lead-based solid solutions—PZN-PT, PMN-PT, and PZN–PMN-PT were synthesized by standard solid state reaction technique. High purity chemicals such as lead oxide [PbO (99.9%, Sigma Aldrich)], magnesium oxide [MgO (99.99%, Sigma Aldrich)], neodymium oxide [Nb_2O_5 (99.9%, Sigma Aldrich)], lead titanate [$PbTiO_3$ (99.99%, Sigma Aldrich)] and zinc oxide [ZnO (99.9%, Alfa Aesar)] were used as starting powders. They were weighted in the stoichiometric molar ratio according to the following chemical Eq. 0.955 Pb $(Mg_{1/3}Nb_{2/3})O_3$–0.045 $PbTiO_3$, 0.955 Pb $(Zn_{1/3}Nb_{2/3})O_3$–0.045 $PbTiO_3$ and 0.462 Pb $(Zn_{1/3}Nb_{2/3})O_3$–0.308 Pb $(Mg_{1/3}Nb_{2/3})O_3$–0.23 $PbTiO_3$. The appropriate amounts of these precursor oxides were mixed and crushed by planetary ball-mill unit (FRITSCH 'Pulverisette 5') with a rotation speed of 200 rpm min^{-1} in a polyethylene container using ZrO_2 balls as grinding agent for 15 h using ethanol as the wetting agent. The mixed powders were dried and pre-sintered at 100 °C in a platinum crucible for 24 h in a muffle furnace to remove the moisture from the sample. Well, mixed and dried powders of raw materials were calcinated at 900 °C for 4 h in the platinum crucible. The calcined powders were mixed with 5 mol% polyvinyl alcohol [PVA] to reduce the brittleness and enhance compactness. The powders were pressed into pellets of size 12 mm diameters and 1–2 mm thickness by cold isostatic pressure technology using tungsten carbide dye. The pressed pellets were sintered at 1200 °C in the tubular furnace for 4 h in covered alumina crucible in order to avoid decomposing of PbO. The sintered samples were polished to a thickness of ~ 0.6 mm and coated with conductive silver paste (code No. 1337-A, Elteck Corporation, India) on both sides as electrodes and then fired at 500 °C for 5 h to remove the solvent and epoxy. Enough care was taken in heating the samples to avoid the formation of cracks and blistering in the pellets. Detailed steps involved in the synthesis and preparation of solid solutions were illustrated in the flow chart given in Perumal et al. [34].

2.2 Characterization techniques

The morphologies of the samples were characterized by a field emission scanning the electronic microscope (FE-SEM, JSM-7001F Japan) with an accelerating voltage of 15 kV. The electric field-induced polarization–electric field (P–E) hysteresis loops were characterized by (radiant

Precision Premier II Technology). The piezoelectric coefficients (d_{33}) of the pellets were measured by a quasi-static method using a Piezometer (YE2730A d_{33} Meter, APC International Ltd). For electrical measurement, the pellets were polled in a silicone oil bath with a direct current (D.C) field at a voltage of 2–4 kV mm^{-1} for 10–30 min from room temperature to 60 °C (Marine India). The temperature dependence of dielectric properties of the solid solutions was investigated using an impedance analyzer (PSM 1735, N4L), where the test frequencies range from 1 to 2 MHz from room temperature to 500 °C. According to the following dielectric formula [9, 16].

$$K_p = \sqrt{2.54 \times \frac{(f_p - f_s)}{f_s}}$$

$$\varepsilon_r = \frac{\varepsilon}{\varepsilon_o} = \frac{Cd}{\varepsilon_o S} = \frac{4Cd}{\varepsilon_o \pi \varphi^2} \approx \frac{144Cd}{\varphi^2}$$

$$Q_m = f_a{}^2 \left[2\pi R_f C f_r (f_a{}^2 - f_r{}^2) \right]^{-1}$$

The free space dielectric constant value ε_0 is 8.85×10^{-12} F m^{-1}, C denotes capacitance (units 10^{-12} F), d denotes the sample thickness (mm), S denotes the area (mm^2), φ denotes the sample diameter. The f_r denotes resonance frequency (Hz), f_a denotes antiresonance frequency (Hz). Q_m denotes the minimum impedance at f_r (ohm) resonance impedance, C denotes capacitance mechanically free at 1 kHz.

3 Results and discussion

3.1 Electric-field-induced polarization

Figure 1 illustrates the polarization vs electric field (P–E) hysteresis loops of (a) PZN-PT, (b) PMN-PT, and (c) PZN–PMN-PT solid solutions at various electric fields of 15, 20, 25, 30, 35, 40, 45, 50, 53 and 57 kV cm^{-1} at room temperature and constant a/c frequency of 50 Hz. The phenomenological of saturation polarization P_s, is that its value increases significantly corresponding to the applied electric field to the solid solutions. Higher values of applied voltage caused the samples to undergo a dielectric breakdown. The maximum value of a coercive field (E_c), remanent polarization (P_r) and maximum polarization (P_m) determined from the hysteresis loops are listed in Table 1. The PZN-PT solid solution has saturated P–E loop at $E_{max} = 57$ kV cm^{-1}, which shows the P_m is 20.1 μC cm^{-2}, the remnant polarization (P_r) is 17.5 μC cm^{-2} and the coercive field (E_c) is 36.5 kV cm^{-1} shown in Fig. 1a. Similarly

PMN-PT and PZN–PMN-PT solid solutions have saturated P–E loops at $E_{max} = 40$, 50 kV cm^{-1}, which shows the P_m values are 7.6, 8.72 μC cm^{-2}, the remnant polarization (P_r) values are 5.8, 3.35 μC cm^{-2} and the coercive field (E_c) values are 10.5, 5.92 kV cm^{-1} respectively shown in Fig. 1b, c. In this hysteresis loops, maximum remnant-polarization (P_r) and coercive field (E_c) were acquired in the presence of defect dipoles generated from internal bias field, which resisted and counteracted the effect of an external field. This corresponds to a significant decrease in both P_r and E_c values which resulted in a slight pinched-type loop with relatively small remnant polarization. The variation in hysteresis parameters might be due to the domain growth and domain rotation/alignment, which take place in the direction of the applied electric field. P–E loops for PZN-PT, PMN-PT, and PZN–PMN-PT solid solutions were shown in Fig. 1a–c and corresponding dependencies of P_r and E_c on E_{max} were summarized inset respectively. The variation of ΔP ($= P_{max} - P_r$) as a component of different electric fields are demonstrated in Fig. 1d. In lead-based solid solutions, nonergodic relaxor (NR) phase was irreversibly changed into normal ferroelectrics with the influence of the electric field. The low estimations of ΔP (6.4 μC cm^{-2}) at 40 kV cm^{-1} was observed since a significant part of the energy is consumed by domain switching and it gets stored as a remanence in ferroelectric solid solutions. P_r decays drastically due to the reversibility of the transformation between ergodic and long-range ferroelectrics while increasing lead content.

P–E hysteresis loops for PZN-PT, PMN-PT, and PZN–PMN-PT at different temperatures are illustrated in Fig. 2a–c. The relaxor characteristics have been measured at various temperatures of 25, 50, 75 and 100 °C at constant ac frequency of 50 Hz. Temperature dependence of remnant polarization P_r, coercive field E_c, internal bias field E_i were evaluated using the following equation [35, 36].

$$E_C = \frac{E_C{}^+ - E_C{}^-}{2}, \ E_i = \frac{E_C{}^+ + E_C{}^-}{2}$$

where $E_c{}^+$ and $E_c{}^-$ denotes convergences of the hysteresis loops with abscissa axis in the positive and negative directions. The remanent polarization almost remains the same before the morphotropic phase boundary (T_{mpb}) and showed a persistent reduction afterward's illustrating its possible application in the high-temperature field. In addition, the coercive field also diminishes as the temperature increments to T_C. Ferroelectric parameters like coercive field (E_c), remanent polarization (P_r), maximum polarization (P_m) and internal bias field E_i function of temperature can be obtained; from the P–E loops are listed in Table 2. When the temperature is low, the hysteresis loop of PZN-PT, PMN-PT, and PZN–PMN-PT is asymmetric, indicative of high E_i in the solid solutions [37, 38]. With increasing temperature, the
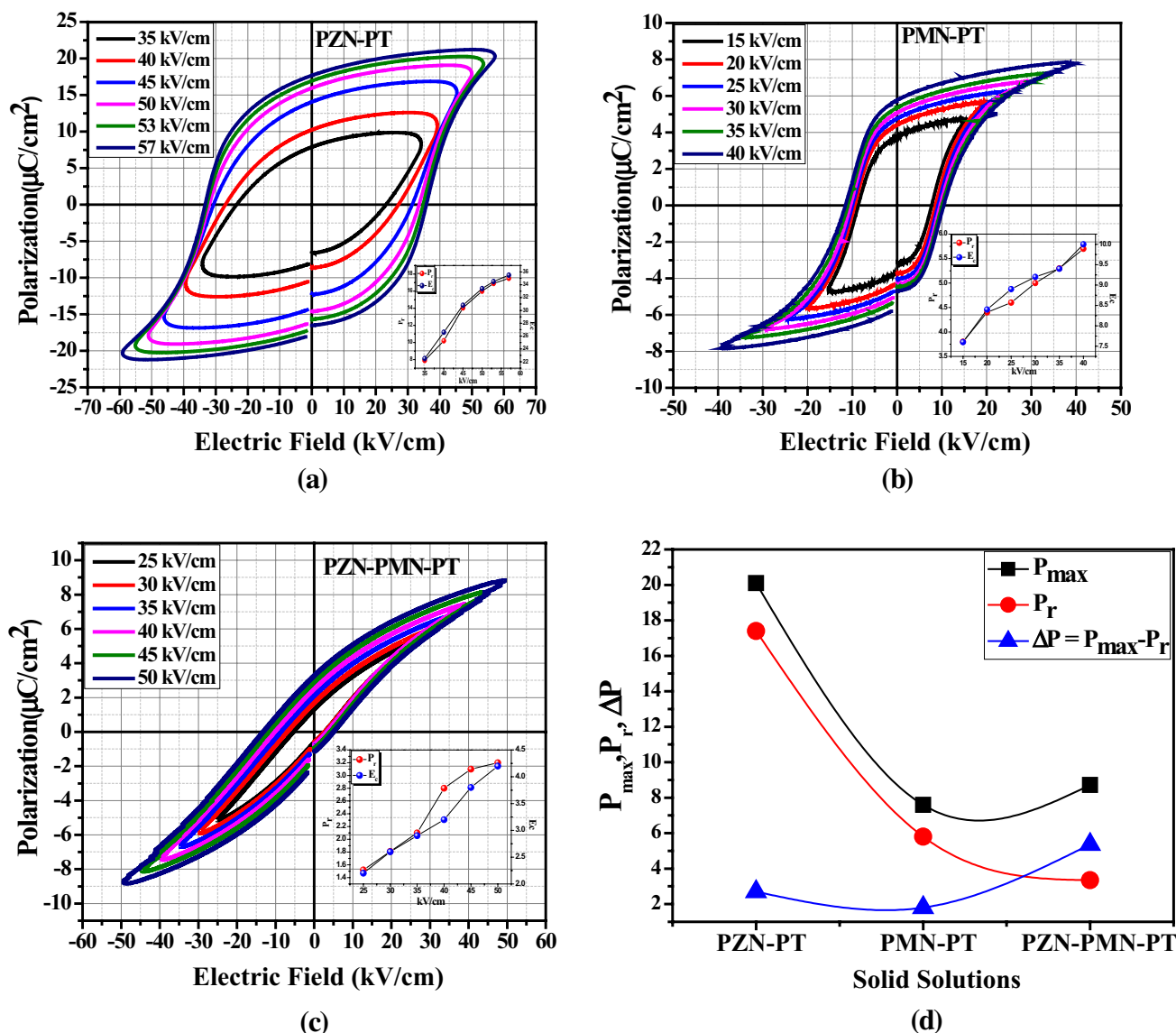
Fig. 1 Ferroelectric hysteresis loops for the **a** PZN-PT, **b** PMN-PT **c** PZN–PMN-PT solid solutions measured at different electric fields at room temperature and **d** the variation tendency of P_{max}, P_r and ΔP

Table 1 Observed electrical parameter for PZN-PT, PMN-PT, and PZN–PMN-PT solid solutions

Solid solutions	d_{33} (pC N^{-1})	g_{33} (mV m N^{-1})	P_m (μC cm^{-2})	E_C (kV cm^{-1})	P_r (μC cm^{-2})	W (J cm^{-3})	η (%)	Dielectric constant (ε_r)
PZN-PT	468	7.78	20.1	36.5	17.4	0.16	45	5132
PMN-PT	324	4.57	7.6	10.5	5.8	0.11	22	6043
PZN–PMN-PT	376	1.66	8.72	5.92	3.35	0.25	71	1925

Piezoelectric constant (d_{33}), maximum polarization (P_m), coercive field (E_C), remnant polarization (P_r), work density (W), dielectric constant (ε_r)

hysteresis loop becomes more symmetric, demonstrating the decrease of E_i, as given in Fig. 2d. The hysteresis loops are symmetric with low levels of temperature, revealing weak E_i

in the solid solutions. Reductions in ferroelectric parameters with the increase in temperature were observed for PZN-PT, PMN-PT and PZN–PMN-PT solid solutions. The weak
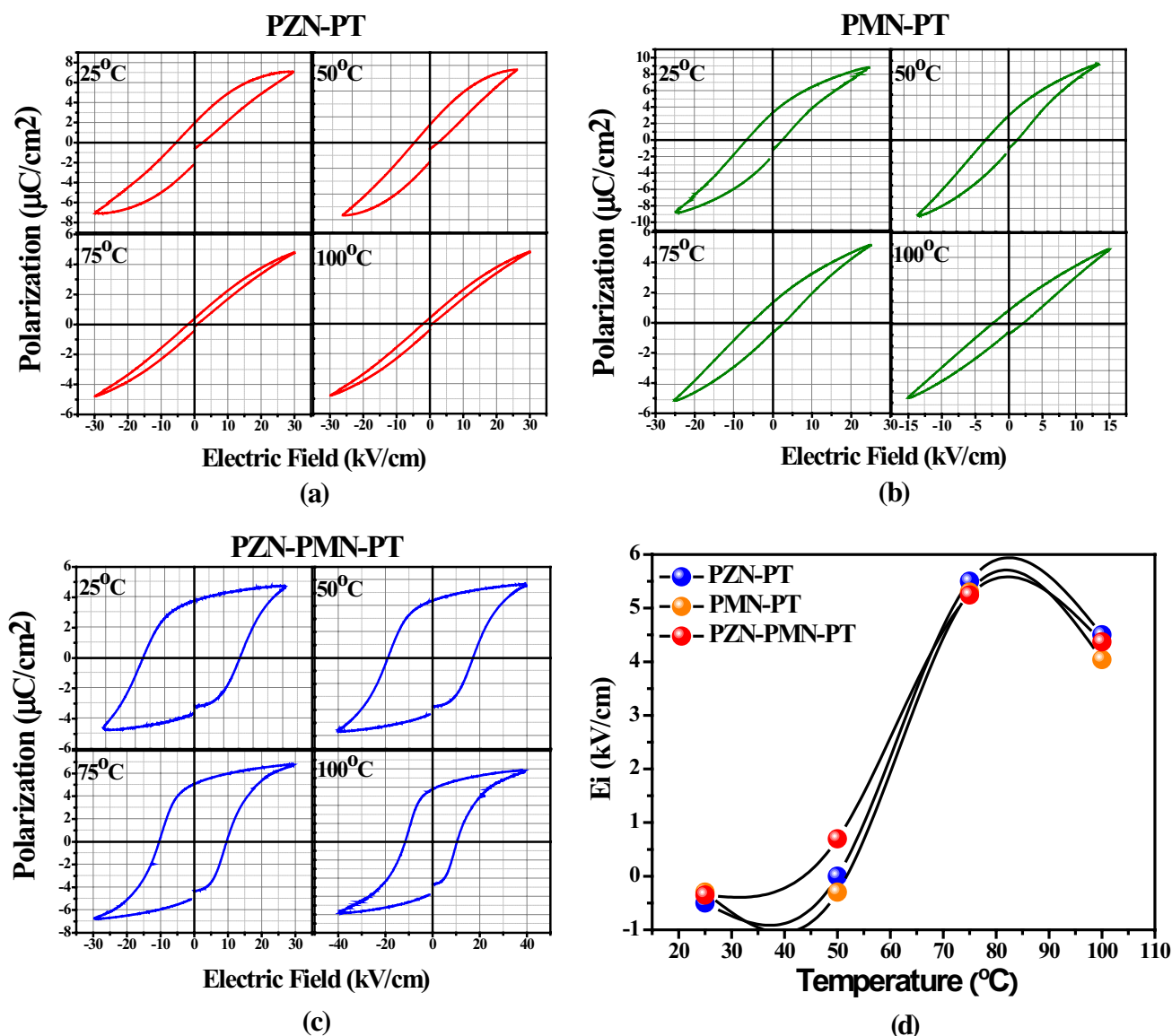
Fig. 2 Temperature-dependent P–E hysteresis loops of **a** PZN-PT, **b** PMN-PT, **c** PZN–PMN-PT solid solutions and **d** (E_i) internal bias field for the PZN-PT, PMN-PT, and PZN–PMN-PT solid solutions

Table 2 Ferroelectric parameters of PZN-PT, PMN-PT and PZN–PMN-PT solid solutions as a function of temperature

Sample name	Ferroelectric response	Temperature (°C)			
		25	50	75	100
PZN-PT	P_r ($\mu C\ cm^{-2}$)	1.9	1.5	0.2	0.0
	P_s ($\mu C\ cm^{-2}$)	6.9	5.4	4.7	4.3
	E_c ($kV\ cm^{-1}$)	6.1	4.5	1.3	0.8
PMN-PT	P_r ($\mu C\ cm^{-2}$)	3.0	2.1	1.2	0.6
	P_s ($\mu C\ cm^{-2}$)	9.1	6.7	5.0	3.3
	E_c ($kV\ cm^{-1}$)	5.7	3.7	2.5	2.0
PZN–PMN-PT	P_r ($\mu C\ cm^{-2}$)	3.7	4.4	5.0	5.8
	P_s ($\mu C\ cm^{-2}$)	4.7	5.5	6.5	7.6
	E_c ($kV\ cm^{-1}$)	7.9	8.7	10	10.6

ferroelectric behaviour at increasing temperature demonstrates the vertical or horizontal displacement of a lead in the lattice. The perception of a pinched-type loop at high temperature might be because of the debilitating of NR state and upgrading ergodic relaxor (ER) state [33]. The spontaneous polarizations of polar nanoregions (PNR) were keeping up the ferroelectric behaviour above T_c in relaxor ferroelectrics. The P–E hysteresis of lead-based solid solutions at 25 °C demonstrates an ordinary hysteresis, and the P–E loop behaviour in the critical compositions in lead-based series clearly indicates the nonpolar phases. As the temperature increases to 75 °C, a sharp decrease in remnant polarization P_r and coercive field E_c were observed. The hysteresis loops became pinched with a further increase in temperature to

100 °C, which correspond to the depolarization temperature T_d of the solid solutions, indicating the non-polar phases. The abatement in P_r was related to the reduction of polarization with the temperature increasing. With increasing temperature, the interface vitality of the ferroelectric domains decreases and the domain walls movement becomes easier, which prompts the decrease of the coercive field.

3.2 Energy storage density study

Figure 3a illustrates the energy storage properties of the PZN-PT, PMN-PT, and PZN–PMN-PT solid solutions which were calculated from well saturated bipolar P–E hysteresis loops. The energy storage behaviours of dielectric materials can be

theoretically evaluated according to the following equation [39–41] where

$$W = \int_0^{P_{max}} E dP,$$

$$W_{rec} = \int_{P_r}^{P_{max}} E dP$$
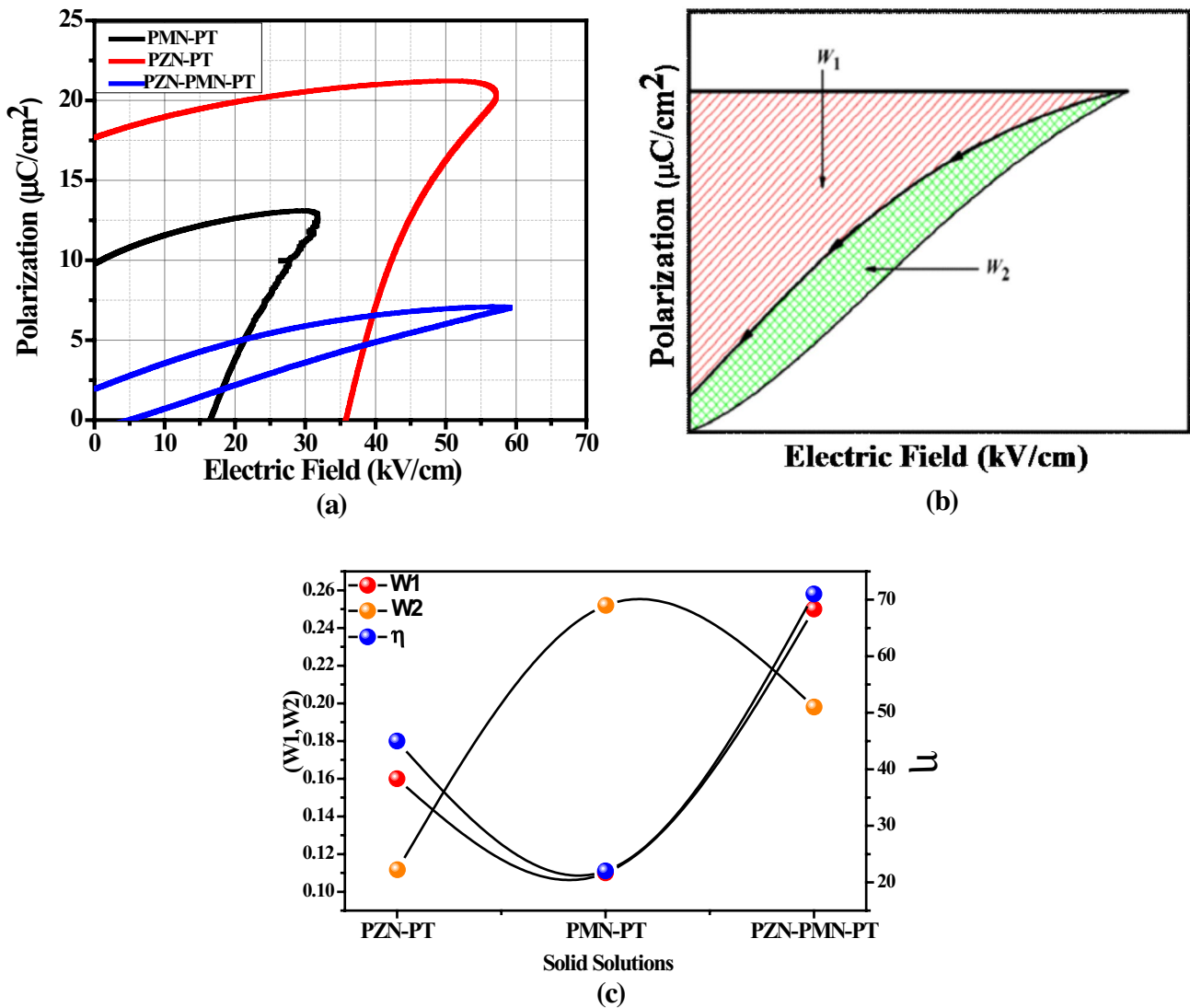
$$\eta = \frac{W_{rec}}{W}$$

Fig. 3 **a** Ferroelectric well saturated bipolar P–E hysteresis loops for PZN-PT, PMN-PT, and PZN–PMN-PT solid solutions, **b** schematic calculation of energy-storage density W_1 and energy loss W_2, **c** theo-retically evaluated the energy-storage density W_1, energy loss W_2 and energy storage efficiency η

Important factors to determine the energy storage performance of the solid solutions: where E is the applied an external field, Pr is the remanence polarization, P_{max} is the maximum polarization, Dp is the change of polarization in the material induced by the applied electric field, η is the energy storage efficiency or charge–discharge efficiency, W is the energy-storage density, W_{rec} is the energy loss

Electric field strength is assessed by integrating the area between the polarization axis and the discharge curveas shown in Fig. 3b [42]. W_{rec} caused by the domain reorientation was calculated by integrating the area between the charge and discharge curve of the unipolar hysteresis loops as shown in Fig. 3b. Larger efficiency means less energy loss during the charge and discharge procession which were theoretically evaluated (W, W_{rec} and η) shown in Fig. 3c. The energy storage density of PZN-PT was ~0.16 J cm^{-3}, PMN-PT was ~0.11 J cm^{-3} and PZN–PMN-PT was ~0.25 J cm^{-3}. From these values it was made clear that implied high magnitudes of permittivity, polarization, and breakdown field will facilitates greater energy density in the dielectric materials due to the reduction in remanent polarization [43, 44]. This result implies that an increase in the energy storage properties leads to a decrease in the ferroelectric phase in the solid solutions.

3.3 Piezoelectric coefficient (d_{33}) and piezoelectric voltage coefficient (g_{33})

Figure 4a, b illustrates the piezoelectric coefficient and piezoelectric voltage coefficient of PZN-PT, PMN-PT, and PZN–PMN-PT solid solutions respectively. The piezoelectric coefficient d_{33} and piezoelectric voltage coefficient g_{33} are defined by the following relations [45–47].

$$d_{33} = \left(\frac{D_S}{T_S}\right)_E = \frac{Q/A}{F/A} = \frac{CV}{F}$$

$$g_{33} = \frac{d_{33}}{\varepsilon_r \varepsilon_o}$$

where, D_S—charge density (C m^{-2}), T_S—mechanical stress (N m^{-2}), E—electric field, C—shunt capacitance, V—potential difference across the shunt capacitor, F—force, A—area of a polled sample, ε_r—dielectric constant, ε_o—dielectric constant in a vacuum

The piezoelectric coefficient for PZN-PT, PMN-PT, and PZN–PMN-PT solid solutions were tabulated in Table 1. It is found that PZN-PT showed better piezoelectric coefficients and piezoelectric voltage coefficients. The high value of d_{33} and g_{33} for PZN-PT was due to the well-developed and aligned grain domains which lead to the large mobility of domain walls. The results showed that apart from changes in the crystal symmetry, microstructure induced domain reconfiguration can also improve the piezoelectric and piezoelectric voltage properties in optimally-doped piezoelectric materials. The ferroelectric domains reorientation more easily during electrical poling and leads to the enhancement of piezoelectric properties. The temperature stability and high piezoelectric coefficient for lead-based solid solutions are experimentally evident in the temperature dependent P–E hysteresis loops for synthesized solid solutions.

In order to check the temperature stability of the piezoelectric properties of the PZN-PT, PMN-PT, and PZN–PMN-PT pellets, measured at room temperature, are plotted against the annealing temperature. The d_{33} value is very stable up to 263 °C for PMN-PT, 412 °C for PZN-PT and 318 °C for PMN–PZN-PT and then drops to zero, which is the Curie
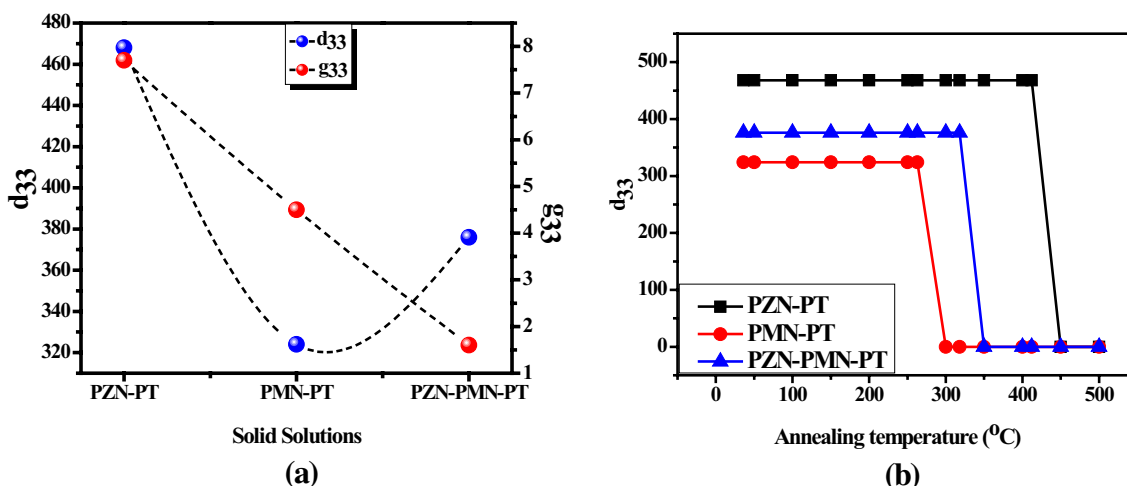

Fig. 4 **a** The d_{33} and g_{33} values of PZN-PT, PMN-PT, and PZN–PMN-PT solid solutions at room temperature, **b** annealing temperature dependence of piezoelectric coefficient d_{33} for PZN-PT, PMN-PT, and PZN–PMN-PT solid solutions

temperature of the solid solutions. The variation of d_{33} with annealing temperature is shown in Fig. 4a. The variation of the d_{33} value is mainly due to the different poling conditions of these three samples. The sample PZN-PT, PMN-PT, and PZN–PMN-PT were poled under the electric field as 2–4 kV mm^{-1}. The difference of the poling electrical field is because of the different breakdown field of each sample. Therefore, the breakdown field of each sample decides the poling field, which can affect the piezoelectric activity. All the samples showed good thermal stability, above which decreases in stability with the increasing temperature were observed. In addition, we found that d_{33} rapidly decreases when the annealing temperature goes above Curie temperature. This phenomenon could be explained by Landau-Devonshire theory [48].

$$T_C = T_O + \frac{3A_4^2}{16A_{20}A_6}$$

$$T_1 = T_O + \frac{A_4^2}{4A_{20}A_6}$$

In this system, the T_0 of all the samples is lower than T_c because of the natures of the first-order phase transition of the solid solutions. So the ferroelectric phase of PZN-PT, PMN-PT, and PZN–PMN-PT solid solution, may exist when $T_a > T_C$.

3.4 SEM micrographs

Figure 5 illustrate the scanning electron microscope (SEM) micrographs of the (a) PZN-PT, (b) PMN-PT, and (c) PZN–PMN-PT solid solutions. It was seen that the PMN-PT, PZN-PT and PMN–PZN-PT solid solutions showed a grain morphology consisting of a mixture of small and large irregularly sized grains with a blend of
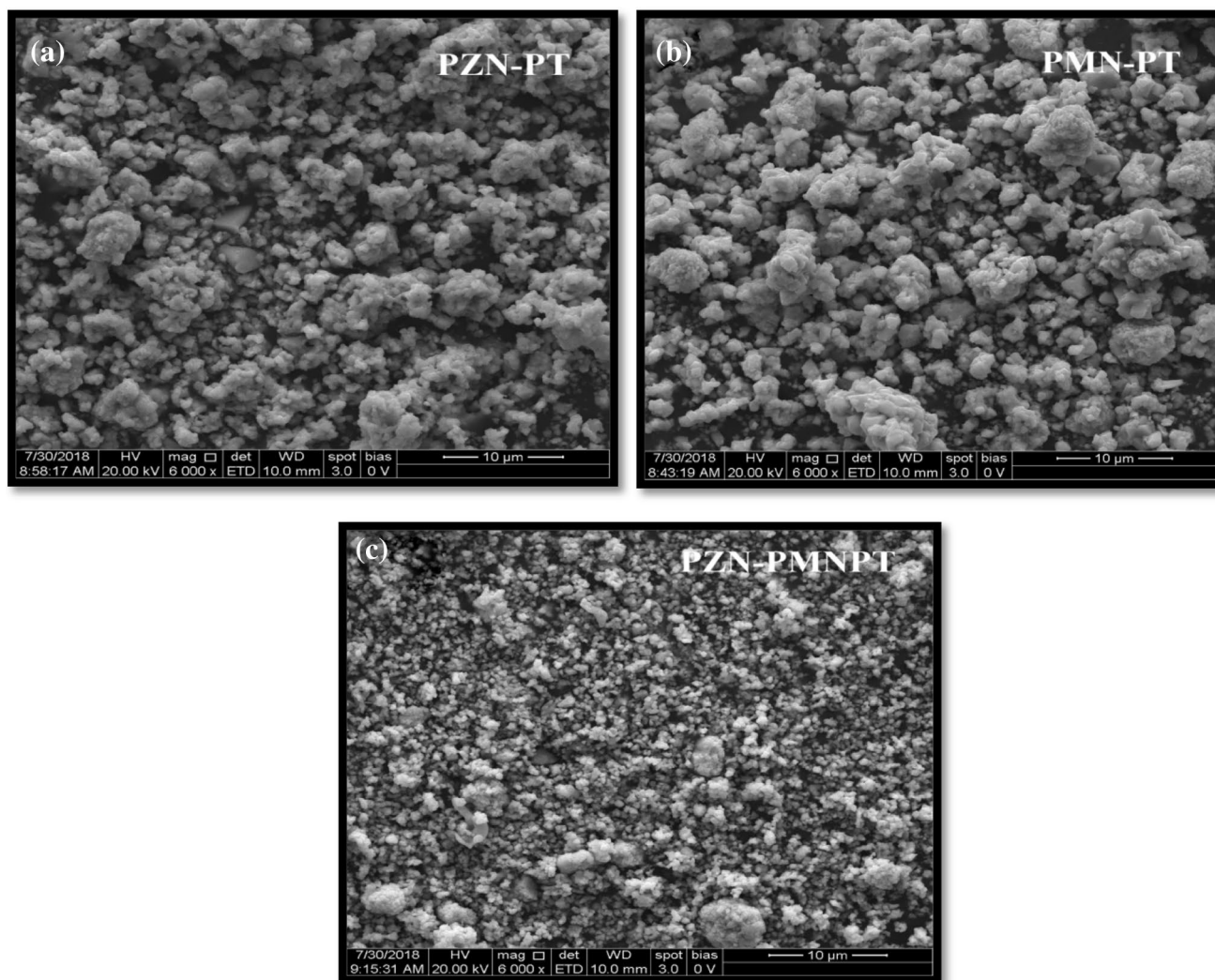

Fig. 5 SEM micrographs of **a** PZN-PT, **b** PMN-PT, and **c** PZN–PMN-PT solid solutions

various shapes. Grains of unequal sizes appear to be distributed throughout the sample. The average grain size observed is about 0.77 μm for PZN-PT, 0.93 for PMN-PT and 1.82 for PZN–PMN-PT solid solutions. Grain sizes were measured and calculated based on a mean linear intercept method. This method was the quantitative measurement of grain size with in dense uniform structures and it was best suited where the boundaries of each grain were relatively easy to determine. A relatively dense morphology and regular grain patterns of the solid solutions lead to higher values of piezoelectric coefficient d_{33}. The ferroelectric domains observed in the micrograph having slightly bigger with more equiaxed grain morphology. The grain size has a great effect on electrical properties such as ferroelectric, dielectric and piezoelectric properties of the solid solution.

3.5 Temperature dependence of dielectric properties

Figure 6 illustrates the variation of the dielectric constant (ε_r) of solid solutions of (a) PZN-PT, (b) PMN-PT and (c) PZN–PMN-PT, respectively, as a function of temperature up to 500 °C at various frequency ranges 1, 5, 10, 50, 100, 500, 1, 1.5 and 2 MHz. Room temperature ε_r were found to be 93,027, 60,611 and 19,341 for PZN-PT, PMN-PT and PZN–PMN-PT, respectively, which increased with temperature and showing a maximum value of 263 °C for PMN-PT, 412 °C for PZN-PT and 318 °C for PMN–PZN-PT. The increase in ε_r with temperature may be due to the dominance of space charge over dipolar polarization. All the solid solutions were showing single structural phase transition. For PMN-PT solid solution shown in Fig. 6b. The ε_r peaks are broad ~ 210–300 °C, similar to the PMN-PT [49, 50] and individual peak positions shifted upward with increasing
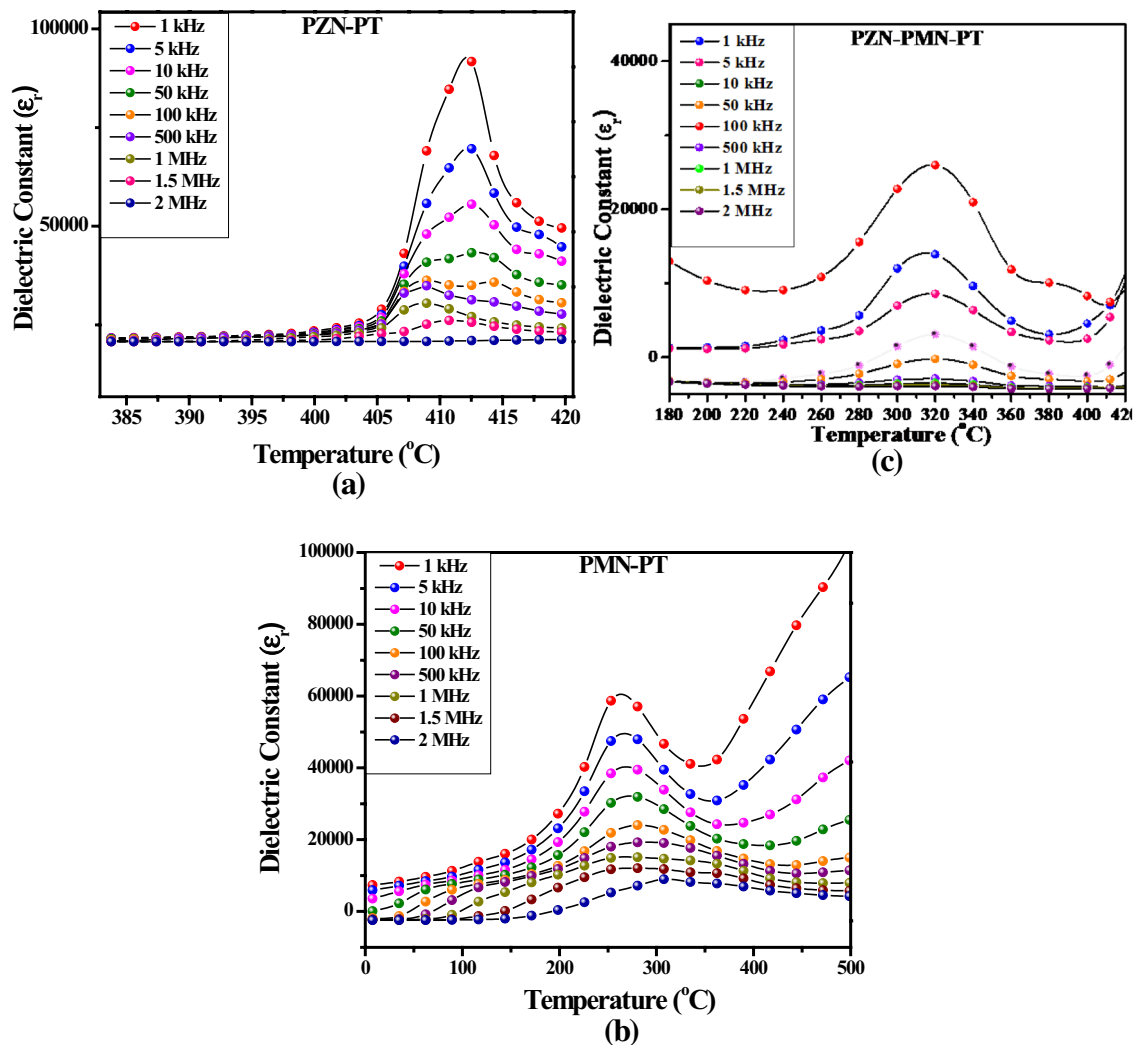

Fig. 6 Temperature dependences of the dielectric constant of **a** PZN-PT, **b** PMN-PT, and **c** PZN–PMN-PT solid solutions

frequency. However, the dielectric spectrum of PZN-PT (shown in Fig. 6a) and PMN–PZN-PT (shown in Fig. 6c.) showed sharp peaks at 360 °C and 320 °C respectively in comparison with PMN-PT (shown in Fig. 6b.). These phase transitions corresponding to T_C are paraelectric cubic phase to a ferroelectric rhombohedral phase [32]. It was more likely that the effect of structures, domains and domain wall motion largely contributed to observed piezoelectric, dielectric and ferroelectric properties.

4 Conclusions

This paper reports the comparison of PZN-PT, PMN-PT, and PZN–PMN-PT solid solutions that were prepared by conventional solid-state reaction technique. Their microstructure, dielectric, piezoelectric, ferroelectric and energy storage behaviour of the solid solutions were investigated. Dielectric studies of the sintered samples were studied as a function of temperature ranging from room temperature to 500 °C and in the wide frequency range of 1–2 MHz which showed good relaxor behaviour. SEM micrographs of the sample showed grains of unequal sizes distribution throughout the sample. The average grain size observed was about 0.77 µm for PZN-PT, 0.93 for PMN-PT and 1.82 for PZN–PMN-PT solid solutions. P–E hysteresis loops for the solid solutions confirmed good ferroelectric properties, exhibiting the values $P_r \sim 17.4, 5.8, 3.35\,\mu C\,cm^{-2}$, $E_c \sim 3.65$, 10.5, 5.92 and $P_m \sim 20.1, 7.6, 8.72$ obtained for PZN-PT, PMN-PT and PZN–PMN-PT respectively. Improved temperature stability of ferroelectric behaviour was observed in the temperature dependent P–E hysteresis loops as a result of binary, ternary solid solutions. A large energy storage density (W) of 0.25 Jcm^{-3} was achieved at 50 kV cm^{-1} for PZN–PMN-PT. The optimum piezoelectric coefficient and piezoelectric voltage coefficient ($d_{33} \sim 468, 324, 376$ pC N^{-1}, $g_{33} \sim 7.78, 4.57, 1.66$) were measured on the polled samples forPZN-PT, PMN-PT and PZN–PMN-PT respectively. The dielectric, piezoelectric and ferroelectric properties of solid solutions suggests that these solid solutions can be potential piezoelectric candidates for use in capacitor applications.

References

1. Q. Gao, Q. Hu, L. Jin, M.V. Gorev, Dielectric relaxation and phase transition behaviour of (1−x)Pb(Zn$_{1/3}$Nb$_{2/3}$)O$_3$-xBaTiO$_3$ binary solid solutions. Ceram. Int. **44**, 18491–18498 (2018). https://doi.org/10.1016/j.ceramint.2018.07.069

2. T. Garg, A.R. Kulkarni, N. Venkataramani, Influence of PbTiO$_3$ addition on microstructure of (1−x)Pb(Mg$_{1/3}$Nb$_{2/3}$)O$_3$-xPbTiO$_3$ ceramics. AIP Conf. Proc. **1536**, 669–670 (2013). https://doi.org/10.1063/1.4810404

3. P.D. Gio, N.D.V. Quang, T.D. Hieu, T.P. Nam, Development of 0.8 Pb(Zr$_{0.48}$Ti$_{0.52}$)O$_3$-0.2Pb[(Zn$_{1/3}$Nb$_{2/3}$)$_{0.625}$(Mn$_{1/3}$Nb$_{2/3}$)$_{0.375}$]O$_3$ ceramics for high-intensity ultrasound applications. J. Electron. Mater. **47**, 5944–5951 (2018). https://doi.org/10.1007/s11664-018-6454-8

4. X. Wang, H. Chen, Dielectric behaviours under high electric field for Pb(Zr$_{1/3}$Nb$_{2/3}$)O$_3$-PbTiO$_3$-BaTiO$_3$ relaxor ferroelectric ceramics. AIP Conf. Proc. **91**, 5979 (2012). https://doi.org/10.1063/1.1466530

5. L.A. Reznitchenko, I.A. Verbenko, O.N. Razumovskaya, Preparation structure and piezoelectric properties of PZN-PMN-PT ceramics in the composition range of large PZN concentrations. Ceram. Int. **38**, 3835–3839 (2012). https://doi.org/10.1016/j.ceramint.2012.01.033

6. J. Peräntie, H.N. Tailor, J. Hagberg, H. Jantunen, Electrocaloric properties in relaxor ferroelectric (1−x)Pb(Mg$_{1/3}$Nb$_{2/3}$)O$_3$-xPbTiO$_3$ system. AIP Conf. Proc. **114**, 174105 (2013)

7. S. Zhang, F. Li, High performance ferroelectric relaxor-PbTiO$_3$ single crystals: status and perspective. AIP Conf. Proc. **111**, 2 (2012). https://doi.org/10.1063/1.3679521

8. N. Wu, X. Song, Y. Hou, Relaxor behavior of (1−x)Pb(Mg$_{1/3}$Nb$_{2/3}$)O$_3$-xPbTiO$_3$ ceramics. Chin. Sci. Bull. **54**, 1267 (2009) https://doi.org/10.1007/s11434-009-0002-0

9. H.W. Zhu, D.Y. Zheng, X.J. Wang et al., Effects of Ta$_2$O$_5$ addition on relaxation behaviour and electric properties of PMS–PNN–PZT ceramics. J. Mater. Sci. Mater. Electron. **29**, 16864–16871 (2018). https://doi.org/10.1007/s10854-018-9781-x

10. S. Patel, A. Chauhan, R. Vaish, Enhancing electrical energy storage density in anti-ferroelectric ceramics using ferroelastic domain switching. Mater. Res. Express **1**, 045502 (2014). https://doi.org/10.1088/2053-1591/1/4/045502

11. J. Li, F. Li, Z. Xu, S. Zhang, Multilayer lead-free ceramic capacitors with ultrahigh energy density and efficiency. Adv. Funct. Mater. (2018). https://doi.org/10.1002/adma.201802155

12. Z. Liu, T. Lu, J. Ye, G. Wang, X. Dong, R. Withers, Y. Liu, Antiferroelectrics for energy storage applications: a review. Adv. Mater. Technol. (2018). https://doi.org/10.1002/admt.201800111

13. M.V. Talanov, L.A. Shilkina, A.I. Verbenko, L.A. Reznichenko, Impact of Ba^{2+} on structure and piezoelectric properties of PMN–PZN–PNN–PT ceramics near the morphotropic phase boundary. J. Am. Ceram. Soc **98**, 838–847 (2015). https://doi.org/10.1111/jace.13371

14. Z. Qiu, H. Hao, M. Cao et al., Characteristics and structure of Mn-doped (0.6−x)PMT–0.4PT–xPZ (x = 0.2, 0.25) ternary system near morphotropic phase boundary. J. Mater. Sci. Mater. Electron. **29**, 14261–14266 (2018). https://doi.org/10.1007/s10854-018-9559-1

15. X. Li, L. Ai, Z. Wang, Y. Liu, C. He, T. Li, T. Chu, D. Pang, H. Tailor, X. Long, Preparation, structure, and electric properties of the Pb(Zn$_{1/3}$Nb$_{2/3}$)O$_3$–Pb(Yb$_{1/2}$Nb$_{1/2}$)O$_3$–PbTiO$_3$ ternary ferroelectric system ceramics near the morphotropic phase boundary. J. Eur. Ceram. Soc. **33**, 2155–2165 (2013). https://doi.org/10.1016/j.jeurceramsoc.2013.03.013

16. A.D. Polli, F.F. Lange, C.G. Levi, Metastability of the fluorite, pyrochlore, and perovskite structures in the PbO-ZrO$_2$-TiO$_2$ system. J. Am. Ceram. Soc. **83**, 873–881 (2004). https://doi.org/10.1111/j.1151-2916.2000.tb01288.x

17. G. Peng, D. Zheng, C. Cheng, J. Zhang, Effect of rare-earth addition on morphotropic phase boundary and relaxation behaviour of the PNN-PZT ceramics. J. Alloys Compd. **693**, 1250–1256 (2017). https://doi.org/10.1016/j.jallcom.2016.10.079

18. N. Luo, Y. Li, Z. Xia, Q. Li, Progress in lead-based ferroelectric and antiferroelectric single crystals: composition modificatio, crystal growth and properties. CrystEngComm **14**, 4547–4556 (2012). https://doi.org/10.1039/C2CE06430H

19. M. Pham-Thi, C. Augier, H. Dammak, P. Gaucher, Fine grains ceramics of PIN–PT, PIN–PMN–PT and PMN–PT systems: drift of the dielectric constant under high electric field. Ultrasonics **44**, e627 (2006)

20. A.H.B. Kumar, Intrinsic polarization and resistive leakage analyses in high performance 5 piezo-/pyroelectric Ho-doped 0.64PMN-0.36PT binary ceramic. Adv. Powder. Technol. (2018). https://doi.org/10.1016/j.apt.2018.08.012

21. T. Li, X. Li, Z. Wang, Y. Liu, C. He, D. Shen, X. Long, A Pb $(In_{1/2}Nb_{1/2})O_3$-Pb $(Zn_{1/3}Nb_{2/3})O_3$-PbTiO$_3$ ternary ferroelectric system with high T$_c$ and high piezoelectric properties. Mater. Res. **48**, 127–130 (2013). https://doi.org/10.1016/j.materresbull.2012.10.020

22. E. Akça, H. Yilmaz, C. Duran, Processing and electrical properties in lead-based (Pb(Mg$_{1/3}$Nb$_{2/3}$)O$_3$, Pb(Yb$_{1/2}$Nb$_{1/2}$)O$_3$, PbTiO$_3$) systems. J. Am. Ceram. Soc. **93**, 28–31 (2010). https://doi.org/10.1111/j.1551-2916.2009.03357.x

23. K. Chung, J. Yoo, C. Lee, D. Lee, Y. Jeong, Microstructural, dielectric and piezoelectric properties of low-temperature sintering Pb(Co$_{1/2}$W$_{1/2}$)O$_3$-Pb(Mn$_{1/2}$Nb$_{2/3}$)O$_3$-Pb(Zr, Ti)O$_3$ ceramics with the addition of Li$_2$CO$_3$ and Bi$_2$O$_3$. Sens. Actuators A **125**, 340–345 (2006). https://doi.org/10.1016/j.sna.2005.06.018

24. R. Samad, B. Want, Dielectric, ferroelectric and magnetic properties of Pb$_{0.95}$Pr$_{0.05}$Zr$_{0.52}$Ti$_{0.48}$O$_3$-CoPr$_{0.1}$Fe$_{1.9}$O$_4$ ceramic composite. J. Alloys Compd. **715**, 43–52 (2017). https://doi.org/10.1016/j.jallcom.2017.04.246

25. Y. Liu, X. Yang, F. Lai, Z. Huang, X. Li, Z. Wang, Structure and properties of Pb(Lu$_{1/2}$Nb$_{1/2}$)O$_3$-0.2 PbTiO$_3$ relaxor ferroelectric crystal. Mater. Res. **67**, 83–86 (2015). https://doi.org/10.1016/j.materresbull.2015.03.005

26. L.A. Reznitchenko, L.A. Shilkina, O.N. Razumovskaya, Phase equilibrium and properties of solid solutions of PbTiO$_3$-PbZrO$_3$-PbNb$_{2/3}$Mg$_{1/3}$O$_3$-PbGeO$_3$ system. Inorg. Mater. **45**, 173–181 (2009). https://doi.org/10.1134/S0020168509020125

27. X. Hao, J. Zhai, X. Song, J. Yang, Fabrication and characterization of sol-gel derived (100) textured (Pb$_{0.97}$La$_{0.02}$)(Zr$_{0.95}$Ti$_{0.05}$)O$_3$ thin films. J. Am. Ceram. Soc. **92**, 3081–3083 (2009). https://doi.org/10.1111/j.1551-2916.2009.03304.x

28. D. Wang, Y. Li, W. Cao, B. Li, J. Yuan, D. Zhang, Effect of MnO$_2$ addition on relaxor behavior and electrical properties of PMNST ferroelectric ceramics. Ceram. Int. **41**, 9647–9654 (2015). https://doi.org/10.1016/j.ceramint.2015.04.030

29. D. Wang, J. Li, M. Cao, S. Zhang, Effects of Nb$_2$O$_5$ additive on the piezoelectric and dielectric properties of PHT-PMN ternary ceramics near the morphotropic phase boundary. Phys. Status Solidi **211**, 226–230 (2014). https://doi.org/10.1002/pssa.201330203

30. D. Wang, Q. Zhao, M. Cao, Y. Cui, S. Zhang, Dielectric, piezoelectric and ferroelectric properties of Al$_2$O$_3$ and MnO$_2$ modified PbSnO$_3$-PbTiO$_3$-Pb(Mg$_{1/3}$Nb$_{2/3}$)O$_3$ ternary ceramics. Phys. Status Solidi A **210**, 1363–1368 (2013). https://doi.org/10.1002/pssa.201228760

31. D. Goswami, S.K. Medda, G. De, Superhydrophobic films on glass surface derived from trimethylsilanized silica gel nanoparticles. ACS Appl. Mater. Interfaces **3**, 3440–3447 (2011). https://doi.org/10.1021/am200666m

32. Z. Kutnjak, J. Petzelt, R. Blinc, The giant electromechanical response in ferroelectric relaxors as a critical phenomenon. Nature **441**, 956 (2006)

33. Z. Liu, B. Wu, J. Wu, Reduced dielectric loss and high piezoelectric constant in Ce and Mn co-doped BiScO$_3$-PbCe$_x$Ti$_{1-x}$O$_3$-Bi(Zn$_{0.5}$Ti$_{0.5}$)O$_3$ ceramics. Ceram. Int. **44**, 16483–16488 (2018). https://doi.org/10.1016/j.ceramint.2018.06.065

34. R.N. Perumal, V. Athikesavan, P. Nair, Influence of lead titanate additive on the structural and electrical properties of Na$_{0.5}$Bi$_{0.5}$TiO$_3$-SrTiO$_3$ piezoelectric ceramics. Ceram. Int. **44**, 13259–13266 (2018). https://doi.org/10.1016/j.ceramint.2018.04.155

35. D. Wang, M. Cao, S. Zhang, Phase diagram and properties of Pb(In$_{1/2}$Nb$_{1/2}$)O$_3$-Pb(Mg$_{1/3}$Nb$_{2/3}$)O$_3$-PbTiO$_3$ polycrystalline ceramics. J. Eur. Ceram. Soc. **32**, 433–439 (2012). https://doi.org/10.1016/j.jeurceramsoc.2011.08.025

36. D. Wang, M. Cao, S. Zhang, Piezoelectric ceramics in the PbSnO$_3$-Pb(Mg$_{1/3}$Nb$_{2/3}$)O$_3$-PbTiO$_3$ ternary system. J. Am. Ceram. Soc. **94**, 3690–3693 (2011). https://doi.org/10.1111/j.1551-2916.2011.04857.x

37. D. Wang, M. Cao, S. Zhang, Investigation of ternary system Pb(Sn, Ti)O$_3$-Pb(Mg$_{1/3}$Nb$_{2/3}$)O$_3$ with morphotropic phase boundary compositions. J. Eur. Ceram. Soc. **32**, 441–448 (2012). https://doi.org/10.1016/j.jeurceramsoc.2011.08.038

38. D. Wang, M. Cao, Q. Zhao, Y. Cui, S. Zhang, Dielectric and piezoelectric properties of manganese-modified PbHfO$_3$-PbTiO$_3$-Pb(Mg$_{1/3}$Nb$_{2/3}$)O$_3$ ternary ceramics with morphotropic phase boundary compositions. Phys. Status Solidi **7**, 221–223 (2013). https://doi.org/10.1002/pssr.201206508

39. I.V. Ciuchi, L. Mitoseriu, C. Galassi, Antiferroelectric to ferroelectric crossover and energy storage properties of (Pb$_{1-x}$La$_x$) (Zr$_{0.90}$Ti$_{0.10}$)$_{1-x/4}$O$_3$ (0.02 ≤ x ≤ 0.04) ceramics. J. Am. Ceram. Soc. **99**, 2382–2387 (2016). https://doi.org/10.1111/jace.14246

40. D. Wang, Z.F.D. Zhou, A. Khesro, S. Murakami, I.M. Reaney, Bismuth ferrite-based lead-free ceramics and multilayers with high recoverable energy density. J. Mater. Chem. A **6**, 4133–4144 (2018). https://doi.org/10.1039/c7ta09857j

41. Y. Pu, L. Zhang, Y. Cui, M. Chen, High energy storage density and optical transparency of microwave sintered homogeneous (Na$_{0.5}$Bi$_{0.5}$)$_{(1-x)}$Ba$_x$Ti$_{(1-y)}$Sn$_y$O$_3$ ceramics. ACS Sustain. Chem. Eng. **6**, 6102–6109 (2018). https://doi.org/10.1021/acssuschemeng.7b04754

42. D.J. Shin, J. Kim, J.H. Koh, Piezoelectric properties of (1-x)BZT-xBCT system for energy harvesting applications. J. Eur. Ceram. Soc. **38**, 4395–4403 (2018). https://doi.org/10.1016/j.jeurceramsoc.2018.05.022

43. D. Wang, Z. Fan, W. Li, High energy storage density and large strain in Bi(Zn$_{2/3}$Nb$_{1/3}$)O$_3$-doped BiFeO$_3$-BaTiO$_3$ ceramics. ACS Appl. Energy Mater. **1**, 4403–4412 (2018). https://doi.org/10.1021/acsaem.8b01099

44. R.A. Malik, A. Hussain, M. Acosta, J. Daniels, Thermal-stability of electric field-induced strain and energy storage density in Nb-doped BNKT-ST piezoceramics. J. Eur. Ceram. Soc. **38**, 2511–2519 (2018). https://doi.org/10.1016/j.jeurceramsoc.2018.01.010

45. R. Rianyoi, R. Potong, A. Ngamjarurojana, Poling effects and piezoelectric properties of PVDF-modified 0–3 connectivity cement-based/lead-free 0.94(Bi$_{0.5}$Na$_{0.5}$)TiO$_3$–0.06BaTiO$_3$ piezoelectric ceramic composites. J. Mater. Sci. **53**, 345–355 (2018). https://doi.org/10.1007/s10853-017-1533-4

46. Q. Guo, G.Z. Cao, I.Y. Shen, Measurements of piezoelectric coefficient d$_{33}$ of lead zirconate titanate thin films using a mini force hammer. J. Vib. Acoust. **135**, 011003 (2013). https://doi.org/10.1115/1.4006881

47. Chitra, K.C. Singh, Dysprosium doping on structural and electrical properties of lead free (Ba$_{0.7}$Ca$_{0.3}$)(Ti$_{0.92}$Sn$_{0.08}$)O$_3$ ceramic system. J. Mater. Sci. Mater. Electron. **29**, 17630–17637 (2018). https://doi.org/10.1007/s10854-018-9866-6

48. S. Lin, T. Lu, C. Jin, Size effect on the dielectric properties of BaTiO$_3$ nano ceramics in a modified Ginsburg-Landau-Devonshire

thermodynamic theory. Phys Rev B **74**, 134115 (2006). https://doi.org/10.1103/PhysRevB.74.134115

49. A. Hussain, N. Sinha, S. Bhandari, H. Yadav, B. Kumar, Synthesis of $0.64Pb(Mg_{1/3}Nb_{2/3})O_3$-$0.36PbTiO_3$ceramic near morphotropic phase boundary for high performance piezoelectric, ferroelectric and pyroelectric applications. J. Asian Ceram. Soc. (2016). https://doi.org/10.1016/j.jascer.2016.06.004

50. N. Abid Hussain, S. Sinha, Goel, B. Kumar, Improvement in dielectric, piezoelectric and ferroelectric properties of 0.64PMN-0.36PT ceramics by Sb modification. J. Mater. Sci. Mater. Electron. **28**, 14298–14307 (2017). https://doi.org/10.1007/s10854-017-7289-4